

# Chemical Bond Formation and Rupture Processes: An Application of DFT-Chemical Pressure Approach

Hussien H. Osman,<sup>†,‡,§,\*</sup> Juan Andrés,<sup>‡</sup> Miguel A. Salvadó,<sup>†</sup> and J. Manuel Recio<sup>†</sup>

<sup>†</sup>MALTA-Consolider Team and Departamento de Química Física y Analítica, Universidad de Oviedo, E-33006, Oviedo, Spain

<sup>‡</sup>Department of Physical and Analytical Chemistry, UJI- Universitat Jaume I, Av. de Vicent Sos Baynat, s/n, Castelló de la Plana 12071, Spain

<sup>§</sup>Department of Chemistry, Faculty of Science, Helwan University, Ain-Helwan, 11795, Cairo, Egypt

---

**ABSTRACT:** Very recently, we have analyzed the nature of chemical interactions in a wide variety of molecules and materials using the Chemical Pressure (CP) approach. We have shown how this newly developed formalism can be used to identify and visualize different types of chemical bonds based on the attractive and repulsive forces between the constitutive atoms of molecules and materials. In this article, we illustrate the capability of the CP approach to clearly track the bond formation and rupture processes in crystalline solids. Using the Indium Phosphide (InP) crystal as a model system, the evolution of its chemical bonding network is investigated in two different phenomena: (i) along a pressure-induced phase transition mechanism and (ii) after electron beam irradiation of the unit cell. The CP maps show distinctive features related to the local atomic interactions in the crystal structure, providing insights into the chemical nature of any distorted/defective structure throughout these transformation processes. This is accomplished by searching for the appearance/disappearance of absolute minima of negative chemical pressure along bonding interatomic paths and of zero CP contour lines surrounding the metallic atoms.

---

## INTRODUCTION

The chemical bond continues to be the main concept in chemistry for understanding chemical structure, stability, reactivity and many other chemical and physical phenomena of a given material,<sup>1,2</sup> even though questions about the nature of chemical bonds are still highly controversial.<sup>3-5</sup> In crystalline solids, knowledge of chemical interactions is of capital interest due to the fundamental information provided for the electronic distribution and local forces in their stable structures.

In fact, much effort is being invested in the development of new methods aimed at the characterization of chemical bonding using density functional theory (DFT) methodologies. The need to understand the nature of a chemical bond stimulates discussions on many different levels of chemical research about how to reconcile the image derived from approximate theories,<sup>1,6</sup> and that obtained from quantum mechanical calculations.<sup>7</sup> Few studies have been conducted to track the chemical bond changes associated with structural and electronic rearrangements, such as solid-solid phase transformations and increasing the total number of electrons in a bulk structure by simulating the effects of electron irradiation, respectively. It is arguable that the difficulty stems from the complexity of the electronic structure in the transient regime associated with the emergence or breaking of chemical bonds. Understanding these chemical bond rearrangements provides detailed insights into the chemical nature of the above processes.

Quantum chemical approaches intended to unravel the nature of chemical bonding generally rely upon the wave function<sup>8-11</sup> or the electron density.<sup>12,13</sup> Nowadays, alternative computational tools are being developed that are based on the various scalar fields which condense the chemically relevant information obtained from quantum calculations into one single intuitive real-space function. Two of the most illustrative molecular scalar fields are the electron density (Bader's QTAIM)<sup>12</sup> and the electron localiza-

tion function (ELF).<sup>14,15</sup> In addition to the electron population of each atom, QTAIM analysis reveals the atomic interactions in molecular and crystalline systems. This strategy was applied for example to track the atomic charge in systems irradiated with a weak electron beam.<sup>16,17</sup> On the other hand, in a quantitative way, ELF topology analysis is widely applied to understand bond characterization in crystalline solids<sup>18-21</sup> and can be used to track the bond formation process along phase transition mechanisms.<sup>22-24</sup>

The new chemical pressure (CP) approach is based on the interplay between the electron density and the energy decomposition distributed in real space, yielding a valuable scheme in which chemical bonds are described in terms of balanced attractive and repulsive forces that are mapped, respectively, in regions of low and high CP values.<sup>25</sup> Recently, we were able to analyze, visualize and differentiate a range of chemical bonds in a wide variety of molecules and crystalline solids using this approach.<sup>26</sup> In this work, we are interested in exploring the efficiency of this formalism to properly describe the bond formation and rupture processes involved in several phenomena such as phase transitions,<sup>22</sup> and electron irradiation of solids.<sup>16,27</sup> One important challenge for the CP formalism is to prove its performance in understanding and rationalizing the interatomic interactions that take place as a chemical or physical process progresses.

Indium Phosphide (InP) is a suitable model system for exploring the CP features in such processes. It is a popular binary semiconductor that is widely used in the electronic devices.<sup>28-30</sup> The low-pressure stable phase of InP has a zinc-blende (B3) crystal structure. The transition pressure for the zinc-blende (B3)-NaCl (B1) first-order phase transition in InP was reported to be within the range of 9.8-11.2 GPa in several previous works.<sup>31-40</sup> From the electronic point of view, as the B3 phase has four atoms per unit cell while the B1 structure has only two, there are twice as many bands per *k*-points in the B3 phase with respect to B1. Therefore, B3 presents two conduction bands, one associated with a direct emission and a second one with a pseudo-direct one.<sup>41-43</sup> From a

structural point of view, the change in the atomic local coordination from 4 to 6 during the B3-B1 transition will be an intuitive example of the bond formation process. In addition, a pure single-crystalline tetragonal In phase growth on the surface of InP nanorods during the weak electron irradiation process carried out inside a high-resolution transmission electron microscope has been reported.<sup>27</sup> Thus, In-P bonds are broken during the segregation of the pure In metallic phase. These phenomena are challenging examples of the application of the CP method.

The article is organized in three more sections. The crystal structure and computational details used in this study are described in the following section. The third section, where the results are discussed, is divided into two main subsections. The first one discusses the CP features for the bond formation process along the B3-B1 phase transition of InP. The second subsection deals with the CP schemes associated with the In-P bond rupture during the electron irradiation of the InP crystal. By the end of this section, it will have been clearly shown how the CP formalism is able to visualize the bond formation and rupture capturing the distribution of the attractive and repulsive forces. The last section summarizes the main results and conclusions of this work.

## Crystal structure

Different phases of InP and metallic In have been used in our study. B3 and B1 structures of InP are used in exploring the phase transition and determining the transition pressure. This transition has been studied experimentally in many previous works.<sup>6,34,44,45</sup> The B3-B1 transition mechanism has been widely studied theoretically using several transition paths. The body-centered orthorhombic unit cell with space group *Imm2* was reported as the one with the lowest activation barrier for SiC,<sup>46</sup> being a model for the transition in this and other materials.<sup>22-24</sup>

In this work, the phase transition path is described by using the unit cell of a common subgroup of the two end members (*Imm2*) with two formula units per unit cell. In this unit cell, the In atom occupies the 2a (0.0, 0.0, 0.0) position while the P atom occupies the 2b (0.0, 0.5,  $z_c$ ) position where  $z_c$  changes from 0.25 (B3) to 0 (B1) along the transition path. The transition profile is explored using the *Imm2* unit cell at the transition pressure using the normalized transformation coordinate,  $\xi$ , which is defined as  $[z_c - z_c^{B3}] / [z_c^{B1} - z_c^{B3}]$  where  $z_c$ ,  $z_c^{B3}$  and  $z_c^{B1}$  are the z coordinate of the P atom at each point on the transition path, B3 and B1 structures, respectively. On the other hand, we simulate the electron irradiation on the B3 structure by gradually increasing the total number of electrons in the unit cell of the bulk structure from 0 to 10 electrons. Reference CP maps such as the one of the sublattice of In atoms in the B3-InP structure (*fcc*) and the one of an In in *vacuo* atom are used in the analysis of the results.

## Computational Methods

First-principles total energy electronic structure calculations were performed under the formalism of DFT as implemented in the ABINIT program.<sup>47-49</sup> We used the LDA exchange-correlation functional of Goedecker, Teter, and Hutter<sup>50</sup> and Hartswigen-Goedecker-Hutter (HGH) pseudopotentials.<sup>51</sup> The valence electrons of P atom,  $3s^2 3p^3$ , and the In  $4d^{10} 5s^2 5p^1$  semi-core electrons were included in all calculations. Optimization of the corresponding unit cell geometries and atomic positions was performed with the Broyden-Fletcher-Goldfarb-Shanno minimization technique. The structural relaxation was carried out until the maximal forces on the atoms were less than  $5 \times 10^{-5}$  Hartree/Bohr. A cut-off energy of 100 Ha along with Monkhorst-Pack<sup>52</sup>  $k$ -points grids ( $6 \times 6 \times 6$ ) were used to ensure convergence of the total energy within  $10^{-4}$  Ha per atom. The B3-B1 transition profile is constructed at the transition pressure using the *Imm2* unit cell at 26 values of the normalized coordinate ( $\xi$ ). At each  $\xi$  value, the unit

cell parameters are optimized using the fixed atomic coordinates condition.

Moreover, in the electron irradiation calculations, LDA-DFT electronic structure calculations were performed both with the ABINIT code and also using the projector-augmented wave (PAW) and plane wave basis set scheme implemented in the Vienna ab initio simulation package (VASP).<sup>53-55</sup> The automatically generated  $\Gamma$ -centered Monkhorst-Pack meshes and a cut-off energy of 530 eV were used to obtain less than  $10^{-4}$  eV per atom in the total energy convergence. The number of electrons is increased in the bulk structure using keywords **NELECT** (VASP) and **CHARGE** (ABINIT) and then a full optimization is performed. For all the optimized structures with VASP, the atomic charge of both atoms is determined using the Bader partitioning method<sup>12</sup> implemented in the Henkelman group code.<sup>56</sup> The same exchange-correlation functional was applied in all calculations.

The preparation of the raw data for the chemical pressure program is performed as three single-point calculations over a volume change of 3% around the equilibrium unit cell volume. Chemical pressure maps are then created using the Fredrickson group CP program.<sup>57</sup> These CP maps were found to be chemically and physically stable showing equivalent results with respect to different computational details as the choice of exchange-correlation functionals. Unless specifically noticed, all the calculations were performed using the core unwarping method in order to reduce the strong CP features around the atomic cores.<sup>26,57</sup> All the CP maps were visualized with the VESTA program,<sup>58</sup> using appropriate pressure range scales for the color-maps to reveal the CP features around the atomic cores and in the interatomic regions (normally red indicates the highest positive and blue indicates the lowest negative CP).

## RESULTS AND DISCUSSION

**3.1. B3-B1 Phase Transition of InP.** In our static calculations (zero temperature and zero-point energy neglected), the stable crystal phase is the one with the lowest enthalpy. Thus, the standard method for studying the relative stabilities of high pressure phases is based on comparing the enthalpy of different crystal structures in terms of pressure. The B3-B1 transition is accompanied by a volume change. Figure 1 shows the relative enthalpy of the B1 phase with respect to B3 as a function of pressure. The transition pressure ( $p_{tr}$ ) is determined when  $\Delta H = H_{B1} - H_{B3}$  is zero. Our calculated  $p_{tr}$  value (9.67 GPa) agrees with the experimental one which lies in the range of 9.8-11.2 GPa.<sup>31-40</sup>

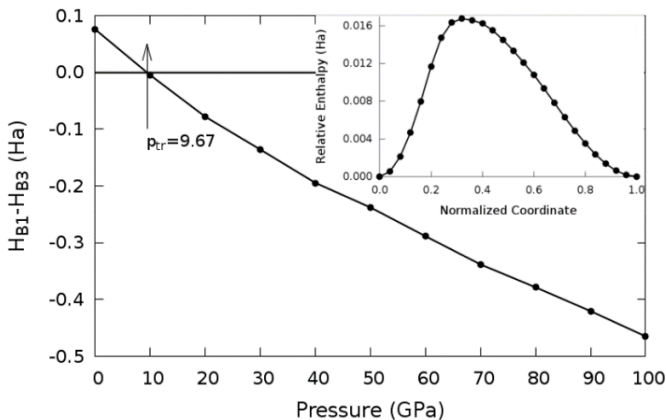


**Figure 1.** Relative enthalpy of B1 to B3 phase of InP versus hydrostatic pressure. The transition pressure is obtained at  $p_{tr} = 9.67$  GPa. The attached inset represents the calculated enthalpy versus the normalized transformation coordinate ( $\xi$ ) at the transition pressure.

The relative enthalpy profile of the *Imm2* cell along the transformation path at the transition pressure is shown in the attached inset of Figure 1. The transition state occurs at  $\xi = 0.32$ . Since the transition happens at  $\xi < 0.5$ , a similarity between the transition state (TS) and the B3 phase is suggested. The coordination number increases from 4 to 6 during the transition from B3 to B1 to form two new In-P bonds. We expect to visualize new CP features for these emerging bonds along the transition path.

The evolution of the cell parameters with the normalized coordinate at the transition pressure is shown in Figure 2. The *b*-axis is the one that is the least affected during the transformation. There is a sudden drop in the *c*-axis from 5.66 Å (at  $\xi = 0$ , B3 phase) to 3.86 Å (at  $\xi = 0.44$ ). A similar trend is obtained for the *a*-axis, with a sudden increase from 3.97 Å (in B3 phase:  $\xi = 0$ ) to 4.97 Å (at  $\xi = 0.44$ ). After  $\xi = 0.44$ , the cell parameters change in a low range until the formation of the B1 phase. The computed cell parameters and cell volumes for the *Imm2* description for B3, transition state (TS), and B1 structures at the transition pressure are collected in Table 1. The total volume is reduced in this transition by about 26%, whereas the volume reduction at the TS is lower than 9% supporting the similarity between B3 and TS structures.

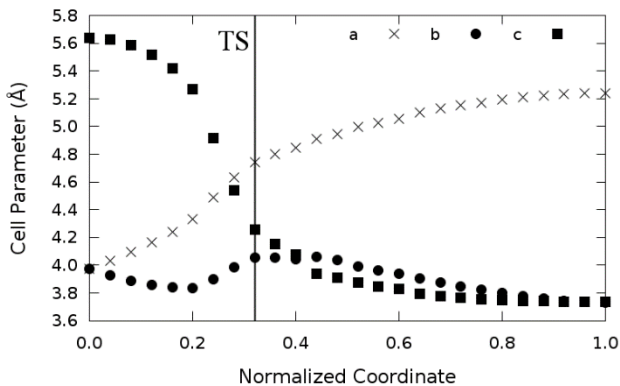


**Figure 2.** Cell parameters of the *Imm2* unit cell versus the normalized transformation coordinate ( $\xi$ ) at the transition pressure.

In terms of the bond distances of the *Imm2* unit cell, there are three different distances that should be tracked in the transformation path. These three distances are between the In atom and three relevant P atoms: equatorial P1, axial P2 and the approaching P3 represented in the 3D unit cell of Figure 3, where the evolution of these distances along the transformation path is presented.

**Table 1.** Calculated structural parameters of the optimized B3, transition state (TS) and B1 structures in the *Imm2* unit cell at the transition pressure. Length is in Angstrom.

	B3	TS	B1
<i>a</i>	3.9750	4.7413	5.2395
<i>b</i>	3.9750	4.0541	3.7366
<i>c</i>	5.6391	4.2576	3.7366
Volume/InP	44.551	40.92	32.97
$\xi$	0.00	0.32	1.00

The equatorial In-P1 distance at  $\xi = 0$  and 1 is 2.437 and 2.640 Å, respectively. The equatorial and axial In-P distances are almost equal and constant along the transition path revealing that the original In-P bonds in the B3 structure are preserved. In contrast, the distance between In and the approaching P3 atoms shows a decreasing trend from a value of 4.6 (  $\xi = 0$ ) to 2.6 Å (  $\xi = 1.0$ ), equal to the bond lengths of In-P1 and In-P2, thus illustrating the formation of new bonds. This trend coincides with the linear trend of the *c*-axis in the previous figure (Figure 2). This axis is associated with the movement of the approaching P atom.

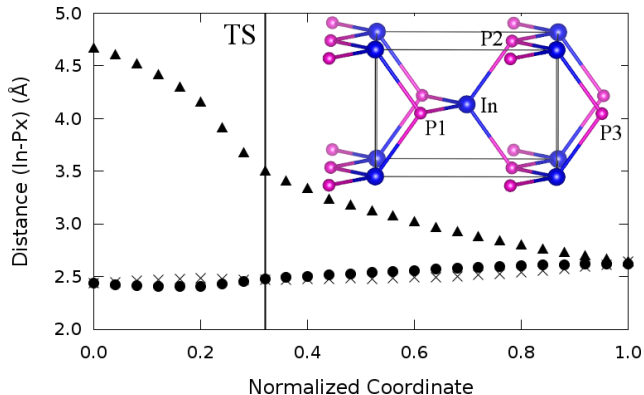


**Figure 3.** The In-P<sub>x</sub> ( $x = 1, 2$  and 3) bond distances in the *Imm2* unit cell as a function of the normalized coordinate along the transformation path. The attached unit cell is for the *Imm2* space group at  $\xi = 0$  including these three distances: equatorial P1 (cross), axial P2 (circle) and the approaching atom P3 (triangle).

Now let us briefly explore the results of applying the CP methodology to the B3-B1 transformation. It is important to identify firstly the CP schemes along the In-P bond and in the interstitial spaces of the starting (B3) and final (B1) structures at  $\xi = 0$  and 1, respectively. The 1D profiles of CP along the equatorial In-P bond are presented in Figure 4a. Overall, the two CP profiles are very similar with a minimum of negative pressure along both In-P bonds. Additionally, the minima along the In-P bonds in the two structures can be visualized using isosurfaces of CP in the 3D representation of Figure 4b. In the two phases, the bonds between the In and P atoms are already confirmed by black disc-shaped features along the interatomic paths. Due to the particular and selected values of the CP isosurfaces, in the B3 phase only these CP features along the bonding path appear, whereas in the B1 phase an additional black isosurface is obtained in the crystal space partially hiding the relevant black disc-shaped entity. Nevertheless, this CP feature will be used as the effective signal for the detection of a new bond.

At  $\xi = 0$  (B3), the CP between the In atom located at the cell center and the approaching P atom (P3 located in the neighboring right unit cell) is very flat. There are no minima or even any special CP features along this direction (Figure 4b-left). In the structure at  $\xi = 1$  (B1), we observe a black disc-shaped feature between the In and P3 atoms, which confirms the bonding that provides the 6-fold coordination of the B1 phase. Such CP features will be used as a reference in our chemical pressure analysis of the rest of the structures along the transformation path.

Now that we have considered the starting and final structures of the B3-B1 transformation, let us briefly explore how other selected structures are reflected in the chemical pressure maps. To focus on the previous essential CP feature, we will look for the onset of the appearance of this black disc-shaped feature between the In atom (at the cell center) and the approaching P3 atom. For this purpose, we present here the most intuitive structures across the

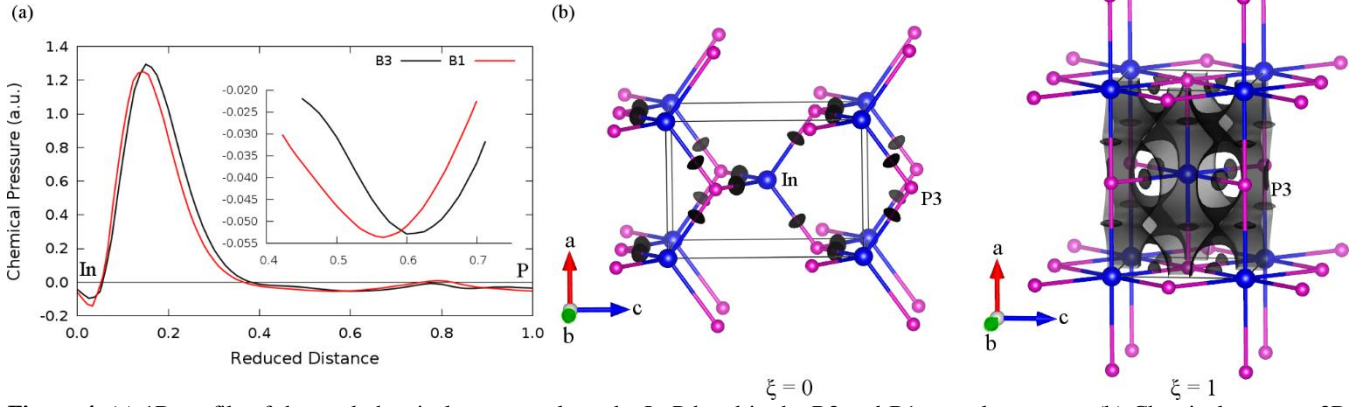


**Figure 4.** (a) 1D profile of the total chemical pressure along the In-P bond in the B3 and B1 crystal structures (b) Chemical pressure 3D isosurfaces of InP (In = blue, P = pink) in B3 and B1 structures in *Imm2* symmetry with CP = -0.043 (left) and CP = -0.051 (right). Pressures are given in atomic units.

transition path showing the evolution of the CP along the expected bond formation path (Figure 5).

The CP between In and the approaching P atom (P3) is always flat up to  $\xi = 0.52$  where a local minimum of CP = -0.05 a.u. appears, a value close to the minimum along the equatorial bonds in the B1 structure (-0.0537 a.u.). The value of this minimum increases gradually (in absolute value) up to the final structure ( $\xi = 1$ ) where it becomes equal to -0.0537 a.u.. These minima are unambiguous signatures of the emergence of new bonds. Clear minima are obtained near the bond centers and have values of -0.0528 a.u. (B3, black) and -0.0537 a.u. (B1, red). In our previous work, this feature indicates the covalent nature of the bond. The minima lie closer to the P atom, thus reflecting the higher electronegativity of the P atom and the polarity of the bond. The maxima near the In core are associated with the  $4d^{10}$  semi-core electrons of the In atoms. The average In-P distance where these minima first appear is 3.153 Å which is longer than the final distance in the B1 structure by about 19%. We propose this value around 3.150 Å as the critical distance for the formation of the new In-P chemical bonds.

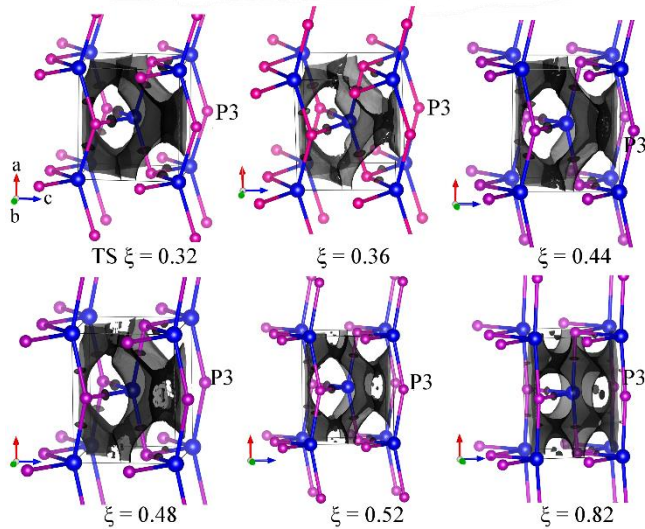


**Figure 5.** Chemical pressure 3D isosurfaces of InP (In = blue, P = pink) in the *Imm2* unit cell at selected  $\xi$  values along the transformation path. CP range from -0.048 to -0.052 a.u.

**3.2. Electron Irradiation of InP.** Irradiation of solids with energetic particles, such as electrons, results in structural and atomic defects that affect the common properties of the material. However, irradiation may have several benefits for the target material. A review of the effects of irradiation on various nanostructured materials has recently been reported.<sup>59,60</sup> In this section, we will demonstrate the effect of electron irradiation on a solid crystal in terms of the CP concept.

We begin with the geometrical optimization of the B3 structure of InP as the number of electrons in the bulk structure increases from  $N = 0$  (neutral) to  $N = 10e_s$  (charged). The volume of the optimized cubic unit cell increases upon adding electrons. The evolution of the optimized cell parameter as a function of the number of electrons is shown in Figure 6. A soft linear trend is obtained up to  $N = 10e_s$ , where the cell becomes almost twice the size of the initial structure ( $a = 10.2$  Å).

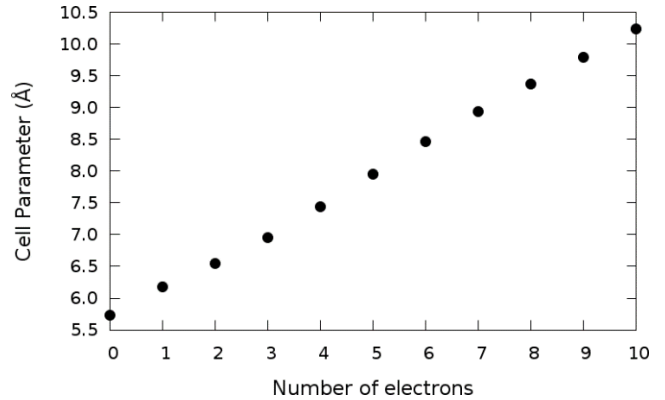


**Figure 6.** Optimized cell parameter of InP crystal versus the number of additional electrons.

Another important variable mainly affected by the irradiation process is the shortest In-P distance. Figure 7 shows the evolution of this bond-length as a function of the net charge of the bulk structure. A linear trend is obtained again up to  $N = 10e_s$ , where the In-P distance becomes too long (4.42 Å) to consider any chemical bond between In and P. Thus, the interatomic interaction decreases considerably due to the electronic defects induced by the irradiation effect within the unit cell.

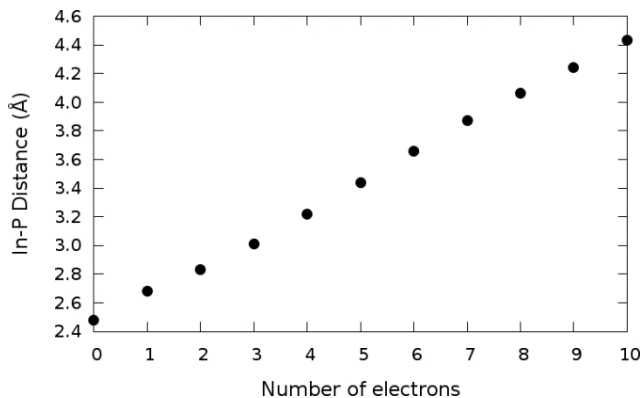


**Figure 7.** In-P distance versus the number of electrons added to the B3-InP structure.

The electronic charge enclosed within the Bader atomic basins was evaluated for the two atom types (In and P) of the B3 structure. We observed that the extra electrons affect the atomic charge of both atoms. Since the B3 phase contains four atoms of each type, each extra electron is shared between the total of eight atoms. The calculated atomic charge of both atoms is represented in Figure 8 as a function of the number of electrons added to the unit cell. A neutral atomic configuration of the In atom is obtained after adding 5 electrons to the bulk structure. Under the same condition, the atomic charge of the P atom becomes -1.25. The analysis of these results reveals that In atoms are the ones that always attract more electrons over the whole irradiation process. Such behavior is attributed to the empty subshells of the outer fifth shell of In atoms (In: [Kr]  $4d^{10} 5s^2 5p^1$ ) and the fact that In is the chemical species acting as a cation in this compound.

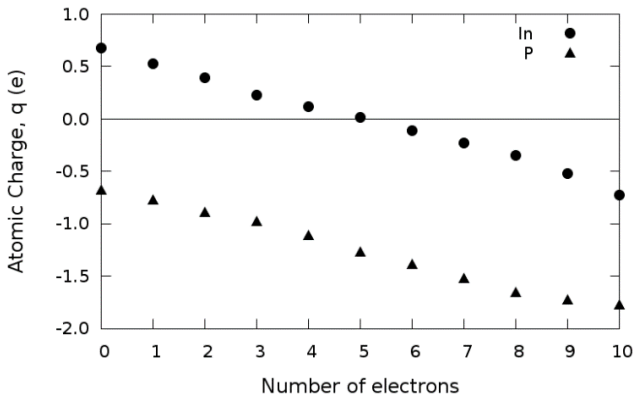


**Figure 8.** Bader atomic charge of In and P atoms versus the number of electrons added to the B3 structure of InP.

The distribution of the additional charge within the unit cell between In and P atoms is shown in Figure 9. It is clear that the incoming electrons are more attracted by In atoms to fill the empty subshells, while the electron distribution percentage for P atoms is always less since the outer subshell is half filled, [Ne]  $3s^2 3p^3$ . In terms of the hard and soft acids and bases principle (HSAB),<sup>61</sup> In and P are categorized as intermediate acid (electron-pair acceptor) and soft base (electron-pair donor), respectively. The electron distribution between the two atoms is very close after  $N = 5e_s$ , where In is neutral becoming soft acid.

Let's move to the chemical pressure results, in which other new features are also apparent. The following representations are the original CP maps, i.e. the core unwarping scheme (used to reduce

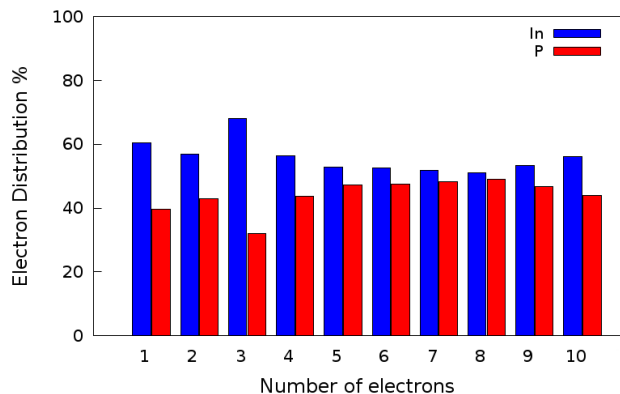


**Figure 9.** Calculated electron distribution of In and P atoms across the electron irradiation of the B3-InP unit cell.

the high CP features around the atomic cores) is not applied in this case. Here we focus on the CP features surrounding the atomic positions considering the distribution of the isolines corresponding to the zero CP. These isolines are used to distinguish the negative and positive pressure regions and are the ones plotted in our 2D maps.

Starting with the 1D-representation, the CP profiles between the two nearest In atoms (black line) and along the In-P bond path (red points) are depicted in Figure 10. Moreover, (101) cross-sections of the CP map containing both In and P atoms are attached. An analysis of the results renders a maximum of positive pressure near the In nuclei which is more intense than in the unwarped case, which is not relevant for the following discussion.

A well of negative pressure appears along the In-P bond path with the minimum displaced to the P position. Here we can also observe this characteristic signature of a polar covalent In-P bond. A feature not visible in the unwarped maps now appears near the In atom, a small maximum delimiting the negative well. The same CP features are also apparent in the attached cross-sections (see 2D CP inset-bottom) in which the In nuclei are surrounded by CP oscillations alternating negative (blue) and positive (red) values. In the 2D CP map (see insets of Figure 10), the interstitial spaces are filled with a flat plateau of low negative pressure.

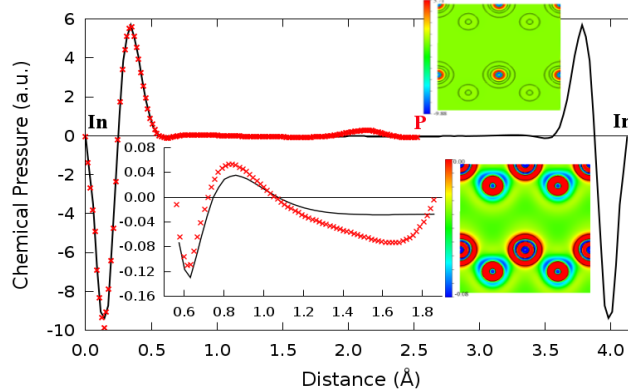


**Figure 10.** 1D chemical pressure profile along the In-In (black line) and In-P (red crosses) interatomic paths calculated for the neutral B3 structure of InP ( $N = 0$ ). Attached insets give zoomed-in views (below) and 2D CP maps along the (101) plane at different CP ranges: original (top) and narrow range (down).

We will now show the CP maps of the irradiated B3-InP crystal and how the CP features change as the number of electrons in the bulk structure increases. We start by visualizing 2D maps of the chemical pressure through the (010) plane containing only In atoms (Figure 11). We can see the effect of adding electrons on

the regions surrounding the atomic cores of In atoms in the crystal. The highest positive pressure (red), located around the In atoms, increases gradually with the addition of extra electrons (CP = +5.69 at  $N = 0$  while CP = +6.86 at  $N = 7e_s$ ). In the neutral structure ( $N = 0$ ), the CP around the In atom is spherical and changes from the lowest negative pressure (blue) to the highest positive pressure (red). The two outer shells are of very low negative and positive pressure as we move toward the neighboring atoms. We can assume that these outer CP shells correspond to the outer valence electrons.

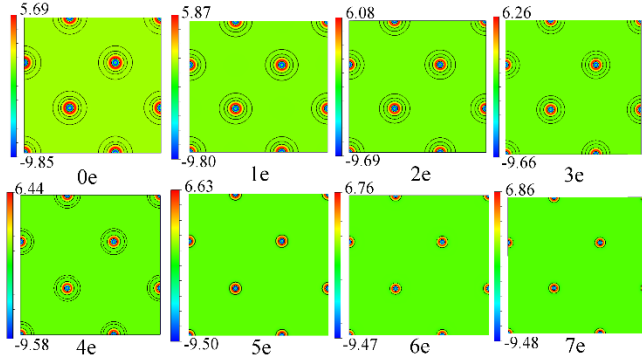


**Figure 11.** Chemical pressure analysis of irradiated B3-InP crystal. 2D cross-sections of the total CP through the plane (010) at different numbers of electrons (from neutral  $N = 0$  to  $N = 7e_s$ ). The CP = 0 contour is shown with a black solid line in all panels.

The CP distribution in these outer shells depends on the number of electrons occupying them. Clearly, the distribution of the contours of CP = 0 is also affected by the irradiation process. It also reflects the interaction with the neighboring atoms. These CP features are changing until the situation of  $N = 5e_s$ , where the two zero CP contour lines disappear, and adding more electrons keeps the In nuclei surrounded only by two contours. According to our calculations analyzed below, this image is similar to the non-interacting image of the isolated system.

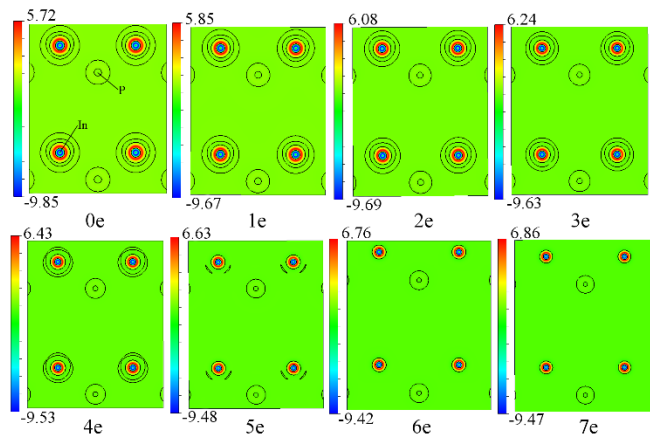


**Figure 12.** Chemical pressure analysis of irradiated B3-InP crystal. 2D cross-sections of the total CP map across the (101) plane at different numbers of electrons (from neutral  $N = 0$  to  $N = 7e_s$ ). The CP = 0 contour is shown with a black solid line in all panels.

New features also appear across the (101) plane that contains both In and P atoms and the bond path (Figure 12). As illustrated in the previous figure, a sudden change in the CP distribution around the In atoms occurs at  $N = 5e_s$ . However, the isolines around the In atoms are not completely spherical as seen through

the (010) plane (Figure 11). This is because of the effect of the chemical bond with P atoms. The CP maps show that the In atoms are more affected than the P atoms by the electron irradiation process. However, it is not possible to easily track the CP distribution along the bond path across these cross-sections due to the high positive pressure near the atomic cores. Thus, to eliminate this effect, the core unwarping step has to be applied (see Figure 13).

In this figure, the minimum along the In-P bond is apparent (inside the dark blue region). The low negative pressure associated with this minimum is located along the bonding region and increases gradually (decreases in absolute value) as new electrons are added. In our previous work, we illustrated how the areas of negative chemical pressure would lower the local energy of the system, indicating a higher interatomic interaction (see Eq. 10 in Ref. 26). This property can be tracked and visualized throughout the irradiation process to obtain information about the bond strength. The progressive increasing of the negative minima of CP indicates weaker In-P interactions as the number of electrons are increased.

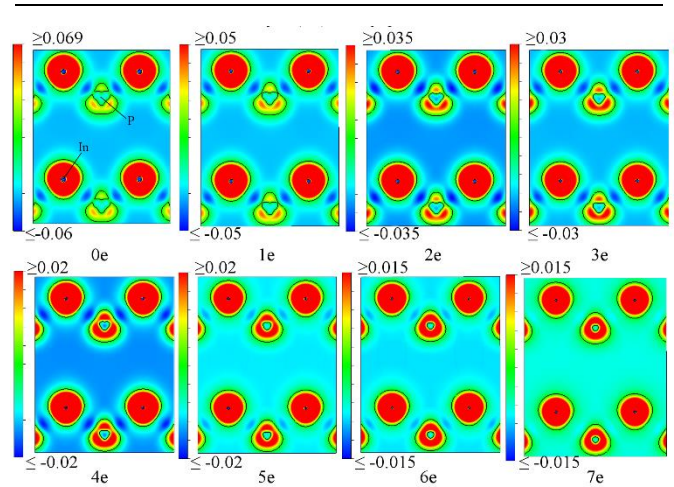


**Figure 13.** Chemical pressure analysis of irradiated B3-InP crystal. 2D cross sections of the total CP across the (101) plane at different number of electrons (from neutral  $N = 0$  to  $N = 7e_s$ ). The CP = 0 contour is shown with a black solid line in all panels.

In the neutral structure ( $N = 0$ ), the In-P bonds are unequivocally established and confirmed. At  $N = 5e_s$ , the In-P distance is longer (see Figure 7) and the CP distribution around the In atoms is different from that in the neutral one (see Figures 11-12). Although weak minima are still present along the In-P contact, these minima do not change anymore even when longer In-P distances are obtained after adding more electrons to the InP unit cell. This scenario suggests a non-interacting environment and allows us to conclude that the In-P bond is broken after irradiating the crystal lattice with 5 electrons.

Incidentally, another advantage of using the unwarping method is that it becomes possible to notice the evolution of the positive CP features around the P atoms as the number of electrons increases. At the neutral structure ( $N = 0$ ), very weak positive CP features are seen around the P nuclei. These features grow as more electrons are added to the unit cell. At  $N > 4e_s$ , the P atoms are surrounded by a continuous outer shell, shown in red, corresponding to the positive CP of the additional charge near the atomic core. Thus, this new feature also delimits the boundary between the scenarios with and without In-P chemical bonds.

To end our analysis, it is very useful to consider how the metallic In crystal and the isolated in *vacuo* In atom are reflected by the

chemical pressure maps. These maps are introduced as a reference for the irradiated InP system. In Figure 14 we illustrate the CP distribution of In metal in the face-centered cubic (*fcc*) structure, the same structure displayed by the In sublattice in the B3 InP phase. The overall CP features are very close to those obtained for other metals in our previous study:<sup>26</sup> the atomic cores are nearly spherical with intense positive pressure. These cores are immersed in a flat plateau of a low negative CP background. The negative and positive pressures average out to zero pressure at the equilibrium geometry. Within the (011) cross-section, the spherical contours of CP = 0 are close to those shown for the neutral ( $N = 0$ ) B3 InP phase (see Figure 11-12).

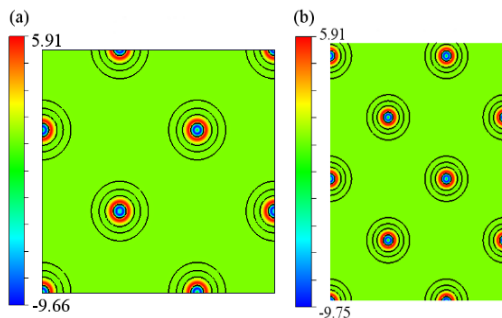


**Figure 14.** Total chemical pressure plots of metallic In in the face-centered cubic (*fcc*) structure across (a) (010) and (b) (101) planes. Black solid contours stand for CP = 0.

Curiously, the image of the metallic In aligns closely to the CP features that have been seen in the CP maps of InP in the B3 structure up to  $N = 5e_s$ . This suggests that the metallic nature is preserved in the In sublattice of InP crystals even under irradiation by electrons provided that the In atoms are still charged. However, in the case of neutral In atoms ( $N = 5e_s$ ), the CP distribution of the metallic sublattice is replaced by other features which are assumed to be associated with the isolate system, as we discussed below.

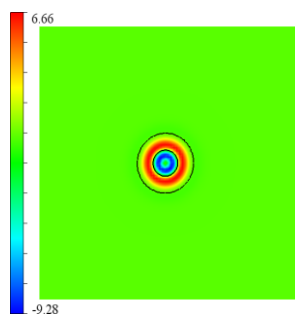


**Figure 15.** Chemical pressure map calculated for an *in vacuo* In atom isolated in a large unit cell ( $a = 10 \text{ \AA}$ ). Cross-section of the total CP containing the nuclear position. Black solid-line curves stand for CP = 0.

The CP distribution of an isolated In atom in a large unit cell is shown in Figure 15 and is consistent with CP maps of a variety of isolated elements shown in previous works (see Figure 2 of Ref. 57). The atomic position at the center of the map is decorated with spherically oscillating pressure features. The outer positive pressure region (red) is associated with the semi-core [ $4d^{10} 5s^2 5p^1$ ] electrons of the In atom. These atomic features are immersed in a flatter, weak negative pressure background. What is important to point out here is that this is the image that coincides with the CP

features obtained in Figures 11-12 for In atoms in the B3 phase when  $N > 4e_s$ .

In summary, as we have illustrated throughout this subsection, a clear signature of the In-P bond-breaking process is the disappearance of the oscillations of the CP associated to outer shells of In. We have also confirmed that the minimum of the CP along the In-P line reaches a constant value, with a concomitant emergence of a continuous positive CP around the P core, when the In-P chemical bond is broken. CP schemes of the metallic and *in vacuo* In atom systems can be used as references to track and detect both the incoming and outgoing states of In along the electronic irradiation process. Thus, the CP analysis allows us to establish a similarity between metallic In and the In sublattice in InP crystal before irradiation as well as between the *in vacuo* In atoms and the segregated In state induced by the electron irradiation when the In-P bond is broken.

## CONCLUSIONS

In the present paper, we have discussed the chemical bond formation/rupture processes from the point of view of the Chemical Pressure (CP) formalism using the InP crystal as a model system. The CP results have been explored and discussed in terms of different representations, including one-, two- and three-dimensional plots. In particular, CP maps are rich in information regarding chemical bonding interactions, attractive and repulsive forces, and atomic sizes. The formation of two new equivalent In-P bonds along the transition path of the B3-B1 phase transition in InP was successfully monitored by this novel CP approach. This was achieved by using a common unit cell of orthorhombic *Imm2* symmetry in which the z coordinate of the P atom is considered as the transformation coordinate. The analysis of the several CP maps created along the transition path allows us to correlate the concentration of negative pressure in the In-P bond path with the presence of a chemical bond. It is clearly shown that the minima of negative pressure (CP = -0.05 a.u.) appear between the In atom and the approaching P atoms (P3 in Figure 5) at  $\xi = 0.52$ . This calculated value gradually increases as the distance between the In and the approaching P atoms decreases along the transition path. At the end of the transition path ( $\xi = 1$ ), the four In-P equatorial bonds have minima of CP of -0.0537 a.u., the same value as the one obtained at the interatomic line between In and the approaching P3 atoms, thus confirming the formation of new bonds. These results can be extrapolated to other binary compounds exhibiting the B3-B1 transformation.

The electron irradiation of the B3 phase of the InP crystal was selected as an example of a bond rupture process. Increasing the total number of electrons in the bulk structure results in augmented In-P distances. The Bader charge analysis shows how the incoming electrons are distributed among the atoms of the crystal. The In atoms attract more electrons in order to fill up their empty subshells and become neutral after adding 5 electrons to the unit cell. In fact, this process induces changes in the CP around the In atoms and along the In-P contacts. Such behavior can be tracked using the isolines of zero CP around the nuclear positions. We have compared the CP maps of the electron irradiated InP B3 phase with those of the metallic and In isolated systems. After adding 5 electrons to the InP crystal, the change in the oscillating behavior of the chemical pressure surrounding the In atoms reveals that the onset of In-P bond rupture leads to the segregation of an atomic isolated In system.

## AUTHOR INFORMATION

### Corresponding Author

\* E-mail: [hokashif@science.helwan.edu.eg](mailto:hokashif@science.helwan.edu.eg)

## Notes

The authors declare no competing financial interest.

## ACKNOWLEDGMENT

H.H.O., M.A.S., and J.M.R. are grateful to the Spanish MINECO and FEDER programs under projects CTQ2015-67755-C2-2-R and Spanish MAT2015-71070-REDC for financial support. J.A. acknowledges financial support from the Generalitat Valenciana for Prometeo/2016/079, the Spanish MINECO for project CTQ2015-65207-P, and Universität Jaume I, project No. UJI-B2016-25.

## REFERENCES

- (1) Pauling, L. *The Nature of the Chemical Bond and the Structure of Molecules and Crystals: An Introduction to Modern Structural Chemistry*; 3rd ed.; Cornell University Press, 1960.
- (2) Weinhold, F.; Landis, C. R. *Valency and Bonding: A Natural Bond Orbital Donor-acceptor Perspective*; Cambridge University Press: Cambridge, UK; New York, 2005.
- (3) Frenking, G.; Shaik, S. *The Chemical Bond: Fundamental Aspects of Chemical Bonding*; vol 2; Wiley VCH, Weinheim, 2014.
- (4) Schmidt, M. W.; Ivanic, J.; Ruedenberg, K. *The Physical Origin of Covalent Bonding*; WileyVCH Verlag GmbH & Co. KGaA, 2014.
- (5) Lewis, G. N. *Valence and the structure of atoms and molecules*; Dover, New York, 1966.
- (6) Mujica, A.; Rubio, A.; Muñoz, A.; Needs, R. High-pressure phases of group-IV, III-V, and II-VI compounds. *J. Rev. Mod. Phys.* **2003**, *75*, 863.
- (7) Gatti C.; Macchi, P. *Modern Charge-Density Analysis*, Springer Dordrecht Heidelberg, London New York, 2012.
- (8) Yannello, V. J.; Kilduff, B. J.; Fredrickson, D. C. Isolobal Analogies in Intermetallics: The Reversed Approximation MO Approach and Applications to CrGa<sub>4</sub>- and Ir<sub>3</sub>Ge<sub>7</sub>-Type Phases. *Inorganic Chemistry* **2014**, *53*, 2730-2741.
- (9) Yee, K. A.; Hughbanks, T. Utility of semilocalized bonding schemes in extended systems: three-center metal-metal bonding in molybdenum sulfide (MoS<sub>2</sub>), niobium tantalum sulfide bronze (Hx(Nb,Ta)S<sub>2</sub>), and zirconium sulfide (ZrS). *Inorg. Chem.* **1991**, *30*, 2321-2328.
- (10) Zurek, E.; Jepsen, O.; Andersen, O. K. Searching for the Interlayer Band and Unravelling the Bonding in  $\beta$ -ThSi<sub>2</sub> and  $\alpha$ -ThSi<sub>2</sub> with NMTO Wannier-like Functions. *Inorg. Chem.* **2010**, *49*, 1384-1396.
- (11) Marzari, N.; Mostofi, A. A.; Yates, J. R.; Souza, I.; Vanderbilt, D. Maximally Localized Wannier functions: Theory and Applications. *Rev. Mod. Phys.* **2012**, *84*, 1419-1475.
- (12) Bader, R. F. W. *Atoms in Molecules: A Quantum Theory*; Oxford University Press: Oxford, England, 1990.
- (13) Johnson, E. R.; Keinan, S.; Mori-Sánchez, P.; Contreras-García, J.; Cohen, A. J.; Yang, W. Revealing Noncovalent Interactions. *J. Am. Chem. Soc.* **2010**, *132*, 6498-6506.
- (14) Becke, A. D.; Edgecombe, K. E. A Simple Measure of Electron Localization in Atomic and Molecular Systems. *J. Chem. Phys.* **1990**, *92*, 5397-403.
- (15) Silvi, B.; Savin, A. Classification of Chemical Bonds Based on Topological Analysis of Electron Localization Functions. *Nature* **1994**, *371*, 683-686.
- (16) Andrés, J.; Gracia, L.; Navarrete, P. -G.; Longo, V. M.; Avansi, W.; Jr.; Volanti, D. P.; Ferrer, M. M.; Lemos, P. S.; La Porta, F. A.; Hernandes, A. C.; Longo, E. Structural and electronic analysis of the atomic scale nucleation of Ag on  $\alpha$ -Ag<sub>2</sub>WO<sub>4</sub> induced by electron irradiation. *Sci. Rep.* **2014**, *4*, 5391.
- (17) Andrés, J.; Gouveia, A. F.; Gracia, L.; Longo, E.; Faccin, G. M.; da Silva, E. Z.; Pereira, D. H.; San-Miguel, M. A. Formation of Ag nanoparticles under electron beam irradiation: Atomistic origins from first-principles calculations. *Int. J. Quantum Chem.* **2018**, *118*, 1-15.
- (18) Savin, A.; Becke, A. D.; Flad, J.; Nesper, R.; Preuss, H.; Von Schnering, H. G. A New Look at Electron Localization. *Angew. Chem.* **1991**, *39*, 409-412.
- (19) Savin, A.; Nesper, R.; Wengert, S.; Fässler, T. F. ELF: The Electron Localization Function. *Angew. Chem., International Edition in English* **1997**, *36*, 1808-1832.
- (20) Kohout, M.; Pernal, K.; Wagner, F. R.; Grin, Y. Electron Localizability Indicator for Correlated Wavefunctions. I. Parallel-spin Pairs. *Theor. Chem. Acc.* **2004**, *112*, 453-459.
- (21) Savin, A. The Electron Localization Function (ELF) and its Relatives: Interpretations and Difficulties. *Journal of Molecular Structure: THEOCHEM* **2005**, *727*, 127-131.
- (22) Salvadó, M. A.; Franco, R.; Pertierra, P.; Ouahrani T.; Recio, J. M. Hysteresis and bonding reconstruction in the pressure-induced B3-B1 phase transition of 3C-SiC. *Phys.Chem.Chem.Phys.* **2017**, *19*, 22887.
- (23) Morales-García, A.; Marqués, M.; Menéndez, J. M.; Franco, R.; Baonza, V. G.; Recio, J. M. A local topological view of pressure-induced polymorphs in SiO<sub>2</sub>. *Theor. Chem. Acc.* **2014**, *133*, 1578.
- (24) Contreras-García, J.; Pendás, A. M.; Recio, J. M. How Electron Localization Function Quantifies and Pictures Chemical Changes in a Solid: The B3  $\rightarrow$  B1 Pressure Induced Phase Transition in BeO. *J. Phys. Chem. B* **2008**, *112*, 9787-9794.
- (25) Fredrickson, D. C. Electronic Packing Frustration in Complex Intermetallic Structures: The Role of Chemical Pressure in Ca<sub>2</sub>Ag<sub>7</sub>. *J. Amer. Chem. Soc.* **2011**, *133*, 10070-10073.
- (26) Osman, H. H.; Salvadó, M. A.; Pertierra, P.; Engelkemier, J.; Fredrickson, D. C.; Recio, J. M. Chemical Pressure Maps of Molecules and Materials: Merging the Visual and Physical in Bonding Analysis. *J. Chem. Theory Comput.* **2018**, *14*, 104-114.
- (27) Golberg, D.; Mitome, M.; Yin, L. W.; Bando, Y. In situ growth of Indium nanocrystals on InP nanorods mediated by electron beam of transmission electron microscope. *Chem. Phys. Lett.* **2005**, *416*, 321-326.
- (28) Zafar, F.; Iqbal, A. Indium phosphide nanowires and their applications in optoelectronic devices. *Proc. R. Soc. A* **2016**, *472*: 20150804.
- (29) Hettick, M.; Zheng, M.; Lin, Y.; Sutter-Fella, C. M.; Ager, J. W.; Javey, A. Nonepitaxial Thin-Film InP for Scalable and Efficient Photocathodes. *J. Phys. Chem. Lett.* **2015**, *6*, 2177-2182.
- (30) Wallentin, J.; Anttu, N.; Asoli, D.; Huffman, M.; Åberg, I.; Magnusson, M. H.; Siefert, G.; Fuss-Kailuweit, P.; Dimroth, F.; Witzigmann, B.; Xu, H. Q.; Samuelson, L.; Deppert, K.; Borgström, M. T. InP nanowire array solar cells achieving 13.8% efficiency by exceeding the ray optics limit. *Science* **2013**, *339*, 1057-1060.
- (31) Nelmes, R. j.; McMahon, M. I.; Belmonte, S. A. Nonexistence of the Diatomic  $\beta$ -Tin Structure. *Phys. Rev. Lett.* **1997**, *79*, 3668.
- (32) Mujica, A.; Needs, R. Theoretical study of the high-pressure phase stability of GaP, InP, and InAs. *J. Phys. Rev. B* **1997**, *55*, 9659.
- (33) Chauvin, N.; Mavel, A.; Patriarche, G.; Masenelli, B.; Gendry, M.; Machon, D. Pressure-Dependent Photoluminescence Study of Wurtzite InP Nanowires. *Nano Lett.* **2016**, *16*, 2926-2930.
- (34) Jamieson, J. C. Crystal Structures Adopted by Black Phosphorus at High Pressures. *Science* **1963**, *139*, 845.
- (35) Menoni, C. S.; Spain, I. L. *Phys. Rev. B*, 1987, *35*, 7520.
- (36) McMahon, M. I.; Nelmes, R. J.; Wright, N. G.; Allan, D. R. Proceedings of the Joint Conference on the AIRATP/APS on High-Pressure Science and Technology, June 28-July 2, 1993, 629.
- (37) Müller, H.; Trommer, R.; Cardona, m.; Vogl, P. Pressure dependence of the direct absorption edge of InP. *Phys. Rev. B* **1980**, *21*, 4879.
- (38) Whitaker, M. F.; Webb, S. J.; Dunstan, D. J. Raman and absorption spectroscopy of InP under high pressure. *J. Phys.: Condens. Matter* **1998**, *10*, 8611.
- (39) Kobayashi, T.; Tei, T.; Aoki, K.; Yamamoto, K.; Abe, K. *Physics of Solids under High Pressure*; (eds Schilling, J. S. et al.) Amsterdam, 1981.
- (40) Ernst, S.; Goñi, A. R.; Syassen, K.; Cardona, M. Plasmon Raman scattering and photoluminescence of heavily doped *n*-type InP near the  $\Gamma$ -X crossover. *Phys. Rev. B* **1996**, *53*(3), 1287.
- (41) Yeh, C.-Y.; Wei, S.-H.; Zunger, A. Relationships between the band gaps of the zinc-blende and wurtzite modifications of semiconductors. *Phys. Rev. B* **1994**, *50*, 2715-2718.
- (42) Signorello, G.; Lörtcher, E.; Khomyakov, P. A.; Karg, S.; Dheeraj, D. L.; Gotsmann, B.; Weman, H.; Riel, H. Inducing a direct-to-pseudodirect bandgap transition in wurtzite GaAs nanowires with uniaxial stress. *Nat. Commun.* **2014**, *5*, 3655.
- (43) Bechstedt, F.; Belabbes, A. Structure, energetics, and electronic states of III-V compound polytypes. *J. Phys.: Condens. Matter* **2013**, *25*, 273201.
- (44) Lukačević, I.; Kirin, D.; Jha, P. K.; Gupta, S. K. Density functional study of stability of high pressure phases in InP and InAs crystals. *Phys. Status Solidi B* **2010**, *247*(2), 273-277.

- (45) Vohra, Y. G.; Weir, S. T.; Ruoff, A. L. High-pressure phase transitions and equation of state of the III-V compound InAs up to 27 GPa. *Phys. Rev. B* **1985**, *31*, 7344.
- (46) Hatch, D. M.; Stokes, H. T.; Dong, J.; Gunter, J.; Wang, H.; Lewis, J. P. Bilayer sliding mechanism for the zinc-blende to rocksalt transition in SiC. *Phys. Rev. B: Condens. Matter Mater. Phys.* **2005**, *71*, 184109.
- (47) Gonze, X.; Jollet, F.; Abreu Araujo, F.; Adams, D.; Amadon, B.; Applencourt, T.; Audouze, C.; Beuken, J. M.; Bieder, J.; Bokhanchuk, A.; Bousquet, E.; Bruneval, F.; Caliste, D.; Côté, M.; Dahm, F.; Da Pieve, F.; Delaveau, M.; Di Gennaro, M.; Dorado, B.; Espejo, C.; Geneste, G.; Genovese, L.; Gerossier, A.; Giantomassi, M.; Gillet, Y.; Hamann, D. R.; He, L.; Jomard, G.; Laflamme Janssen, J.; Le Roux, S.; Levitt, A.; Lherbier, A.; Liu, F.; Lukačević, I.; Martin, A.; Martins, C.; Oliveira, M. J. T.; Poncé, S.; Pouillon, Y.; Rangel, T.; Rignanese, G. M.; Romero, A. H.; Rousseau, B.; Rubel, O.; Shukri, A. A.; Stankovski, M.; Torrent, M.; Van Setten, M. J.; Van Troeye, B.; Verstraete, M. J.; Waroquiers, D.; Wiktor, J.; Xu, B.; Zhou, A.; Zwanziger, J. W. Recent developments in the ABINIT software package. *Comput. Phys. Comm.* **2016**, *205*, 106-131.
- (48) Gonze, X.; Amadon, B.; Anglade, P.-M.; Beuken, J.-M.; Bottin, F.; Boulanger, P.; Bruneval, F.; Caliste, D.; Caracas, R.; Côté, M.; Deutsch, T.; Genovese, L.; Ghosez, P.; Giantomassi, M.; Goedecker, S.; Hamann, D. R.; Hermet, P.; Jollet, F.; Jomard, G.; Leroux, S.; Mancini, M.; Mazevet, S.; Oliveira, M. J. T.; Onida, G.; Pouillon, Y.; Rangel, T.; Rignanese, G.-M.; Sangalli, D.; Shaltaf, R.; Torrent, M.; Verstraete, M. J.; Zerah, G.; Zwanziger, J. W. ABINIT: First-principles Approach to Material and Nanosystem Properties. *Comput. Phys. Commun.* **2009**, *180*, 2582-2615.
- (49) Gonze, X.; Rignanese, G.-m.; Verstraete, M.; Beuken, J.-m.; Pouillon, Y.; Caracas, R.; Raty, J.-y.; Olevano, V.; Bruneval, F.; Reining, L.; Godby, R.; Onida, G.; Hamann, D. R.; Allan, D. C. A Brief Introduction to the ABINIT Software Package. *Z. Kristallogr.* **2005**, *220*, 558-562.
- (50) Goedecker, S.; Teter, M.; Hutter, J. Separable Dual-space Gaussian Pseudopotentials. *Phys. Rev. B* **1996**, *54*, 1703-1710.
- (51) Hartwigsen, C.; Goedecker, S.; Hutter, J. Relativistic Separable Dual-space Gaussian Pseudopotentials from H to Rn. *Phys. Rev. B* **1998**, *58*, 3641-3662.
- (52) Monkhorst, H.; Pack, J. Special Points for Brillouin-zone Integrations. *Phys. Rev. B* **1976**, *13*, 5188-5192.
- (53) Blöchl, P. E. Projector augmented-wave method. *Phys. Rev. B: Condens. Matter Mater. Phys.* **1994**, *50*, 17953-17979.
- (54) Kresse, G.; Furthmüller, Efficient iterative schemes for *ab initio* total-energy calculations using a plane-wave basis set. *J. Phys. Rev. B: Condens. Matter Mater. Phys.* **1996**, *54*, 11169-11186.
- (55) Kresse, G.; Joubert, D. From ultrasoft pseudopotentials to the projector augmented-wave method. *Phys. Rev. B: Condens. Matter Mater. Phys.* **1999**, *59*, 1758-1775.
- (56) Tang, W.; Sanville, E.; Henkelman, G. A grid-based Bader analysis algorithm without lattice bias. *J. Phys.: Condens. Matter.* **2009**, *21*, 084204.
- (57) Berns, V. M.; Engelkemier, J.; Guo, Y.; Kilduff, B. J.; Fredrickson, D. C. Progress in Visualizing Atomic Size Effects with DFT-Chemical Pressure Analysis: From Isolated Atoms to Trends in AB<sub>5</sub> Intermetallics. *J. Chem. Theory Comput.* **2014**, *10*, 3380-3392.
- (58) Momma, K.; Izumi, F. VESTA 3 for Three-dimensional Visualization of Crystal, Volumetric and Morphology data. *J. Appl. Crystallogr.* **2011**, *44*, 1272-1276.
- (59) Krasheninnikov, A. V.; Nordlund, K. *Ion and electron irradiation-induced effects in nanostructured materials.* *J. Appl. Phys.* **2010**, *107*, 071301.
- (60) Gonzalez-Martinez, I. G.; Bachmatiuk, A.; Bezugly, V.; Kunstmann, J.; Gemming, T.; Liu, Z.; Cuniberti, G.; Rummeli, M. H. Electron-beam induced synthesis of nanostructures: a review. *Nanoscale* **2016**, *8*, 11340-11362.
- (61) Pearson, R. G. Hard and Soft Acids and Bases. *J. Am. Chem. Soc.* **1963**, *85*, 3533.

# TOC Graphic

